Materials Science & Engineering A 776 (2020) 138967

Contents lists available at ScienceDirect

Materials Science & Engineering A

journal homepage: http://www.elsevier.com/locate/msea

Microstructure-property relationships in directly aged Alloy 718 turbine disks

F. Theska [a], A. Stanojevic [b], B. Oberwinkler [b], S. Primig [a,*]

[a] School of Materials Science & Engineering, UNSW Sydney, NSW, 2052, Australia
[b] Voestalpine BÖHLER Aerospace GmbH & Co KG, Kapfenberg, Austria

ARTICLE INFO

Keywords:
Alloy 718
Superalloy
Turbine disk
Direct aging
Precipitates
Atom probe microscopy

ABSTRACT

Direct ageing (DA) of forged Alloy 718 turbine disks enables the design of more efficient aircraft engines due to high-temperature yield strength increments of around 10%. This 'DA effect' is related to the dislocation density, δ-phase content and nanoscale γ′- and γ"-precipitate morphology. However, in real turbine disks, local differences in the thermo-mechanical history often deteriorate the DA effect below customers specifications. Thus, the aim of this paper is to unravel the complex microstructural evolution in low-versus high-yield strength regions.

We use hardness mapping, macro-etching, thermo-kinetic and FEM modelling to identify the regions of interest. EBSD, TEM and atom probe microscopy (APM) enable micro- and nanostructure characterization. Low-hardness regions exhibit larger grains, lower δ-phase contents, and lower geometrically necessary dislocation densities. Nanoscale γ′- and γ"-precipitates are coarser, with lower number density, and more complex coprecipitate morphology. We assign the origins of these changes to local temperature and strain conditions during forging, and inhomogeneities in pre-materials.

A proposed microstructural model explains the underlying mechanisms. Local strain-induced δ-phase dissolution results in recovery, recrystallisation and grain growth during forging, reducing the number of nucleation sites for precipitation. Thus, the DA effect deteriorates due to accelerated γ"-precipitate coarsening and less uniform particle dispersions.

1. Introduction

Modern aircrafts are able to cover distances over 14,000 km in a single non-stop flight (e.g. Perth – London) due to recent advances engine design [1,2]. Current efforts to further increase flight distances while reducing travel time require even higher operation temperatures and, thus, advancements in high-temperature materials design [3,4]. Here, advanced processing of established materials represents a rapid and cost-effective response to meet the growing demands for more than 37,000 new aircraft by 2037 [5].

Alloy 718 is a precipitation-hardened, wrought NiFe-based superalloy [6,7]. Comparably low costs and outstanding high-temperature strength make Alloy 718 one of the most common materials for manufacturing of high-pressure turbine disks for aircraft engines [8]. Here, the standard operational temperature is 650 °C for service times of >100,000 h under high mechanical workloads [6,7]. The microstructure of Alloy 718 contains the following main components: A solid solution strengthened face centered cubic (fcc) γ-matrix with a grain size of around ASTM 10 provides optimal high-temperature strength [9,10]. $D0_a$ ordered micrometer-sized δ-phase platelets ($Ni_3(Nb)$) decorate twin and grain boundaries to provide Zener pinning and creep resistance [11]. Ordered nano-scale γ'- ($L1_2$ $Ni_3(Al,Ti)$) and γ"- ($D0_{22}$ $Ni_3(Nb)$) precipitates occur as monoliths, duplets, triplets and quadruplets to provide the high-temperature strength up to 650 °C [9,12]. The key strengthening contributors are coherency and anti-phase boundary (APB) strengthening, which are dominated by the meta-stable, semi--coherent γ"-precipitates [13]. Overaging causes γ"-precipitates to lose coherency to the γ-matrix, deteriorating the high-temperature strength. This effect has been reported to be a precursor for the γ" → δ transformation [14,15].

Currently, Alloy 718 turbine disks are often manufactured following a thermo-mechanical processing route known as direct ageing (DA). This is achieved by omitting solution annealing between forging and ageing in contrast to conventional processing routes [10,16]. DA enables the

* Corresponding author. Hilmer Building (E10), UNSW Sydney, Kensington Campus, NSW, 2052, Australia.
E-mail addresses: f.theska@unsw.edu.au (F. Theska), aleksandar.stanojevic@voestalpine.com (A. Stanojevic), bernd.oberwinkler@voestalpine.com (B. Oberwinkler), s.primig@unsw.edu.au (S. Primig).

https://doi.org/10.1016/j.msea.2020.138967
Received 12 September 2019; Received in revised form 9 January 2020; Accepted 15 January 2020
Available online 24 January 2020
0921-5093/

generation of significant yield strength increments of around +10% at 650 °C, due to changes in micro- (lower grain size and δ-phase fraction) and nanostructure (higher dislocation density, changes in stacking sequence of nanoscale precipitates), as recently reported by some of the current authors [9,12].

The complex industrial manufacturing of Alloy 718 turbine disks requires detailed considerations around the relationships between local temperatures and strain, (T, ϕ) [10]. However, local yield strength variations often cause Alloy 718 turbine disks to fail customer specifications. This is indicative of insufficient process, and thus, microstructure control. Reliable DA requires precise control of temperature, strain, and pre-material. Therefore, in modern process optimization, experimental studies are supported by finite element method (FEM) and thermo-kinetic modelling [10]. Although the impact of thermo-mechanical processing on mechanical properties has been successfully modelled for DA of Alloy 718, the detailed microstructural phenomena have remained largely unknown until recently [9]. Here, modelling-based predictions of local yield strength variations are still limited and, thus, require a more detailed understanding of the microstructural evolution in real turbine disks.

The present work aims to advance our understanding of the complex microstructural evolution in Alloy 718 turbine disks exhibiting both cross-sectional and circumferential yield strength variations. A combination of hardness mapping, light optical microscopy (LOM) with macro-etching, thermo-kinetic and finite element modelling enables the reproducible identification of the regions of interest. Correlative microstructural characterization is carried out for selected high- and low-hardness/yield strength regions using scanning electron microscopy (SEM), electron backscatter diffraction (EBSD), transmission electron microscopy (TEM) and atom probe microscopy (APM). Grain size, δ-phase, geometrically necessary dislocations (GND), and γ′- and γ"-precipitates are thoroughly analyzed using the same methods as published in Refs. [9,17]. Experimental findings are compared to process and microstructure modelling results in order to propose a microstructural model clarifying the origin of these yield strength variations.

2. Material and methods

2.1. Manufacturing of turbine disks

Three industrially manufactured, cross-sectional Alloy 718 turbine disk slices were provided by voestalpine BÖHLER Aerospace GmbH & Co KG, Austria. Disks #1 and #2 were forged to identical geometries with double melt pre-material (vacuum induction melting (VIM), vacuum arc remelting (VAR) followed by homogenization, ingot breakdown and radial forging). To study the influence of disk shape, disk #3 was forged to a slightly different geometry with larger radius from triple melt material (VIM, electro-slag remelting (ESR), VAR followed by homogenization, ingot breakdown and radial forging). All other parameters were identical for all three disks. The chemical composition of Alloy 718 used in this study is given in Table 1.

All disk forging was carried out in two heats I and II at around 1,000 °C as provided in Fig. 1. The initial billet size was h = 400 mm, and d = 250 mm. DA was carried out for 8 h at 720 °C and 620 °C, respectively. Cross-sectional disk slices were cut parallel to the radius and normal to the tangential direction in order to examine radial positions of yield strength variations in circumferential direction as represented in Fig. 2. Regions of interest surrounding yield strength variations were isolated by further cutting the cross-sectional slices into dimensions of ~80 × 110 × 10 mm^3 as shown in Fig. 3.

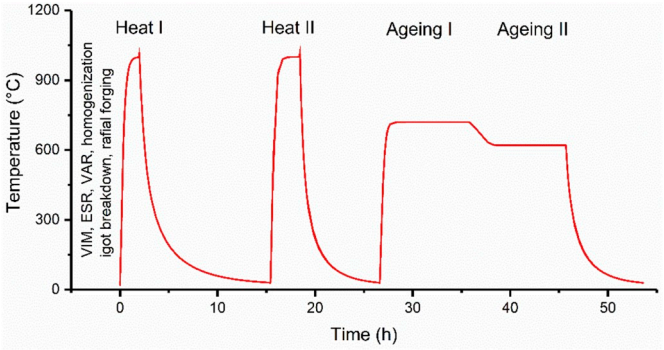

Fig. 1. Time-temperature-forging schedule for forging all three Alloy 718 turbine disks. Two forging heats (Heat I and II) were carried out. 'Direct ageing' (Ageing I and II) followed without solution annealing.

2.2. Microstructure and process modelling

The integrated process modelling procedure developed by Oberwinkler et al. [10] was used to model the manufacturing process. This automated simulation chain uses MATLAB ® integrating the following process steps: Feedstock billets are stored as binary files and DEFORM ® FEM modelling is used to generate the thermo-mechanical history such as temperature and time. MatCalc thermo-kinetic modelling determines phase fractions, precipitate size and their corresponding yield strength contributions over time [18]. A modified thermodynamic and thermo-kinetic database in MatCalc developed at voestalpine BÖHLER Aerospace is used for this purpose. The Bohler Mechanical Properties Postprocessor (BoMePP) enables calculation of additional yield strength contributions to the overall yield strength [10]. Final post-processing and visualization are done via ParaView software packages [19]. FEM point tracking of selected points of interest is used to model the

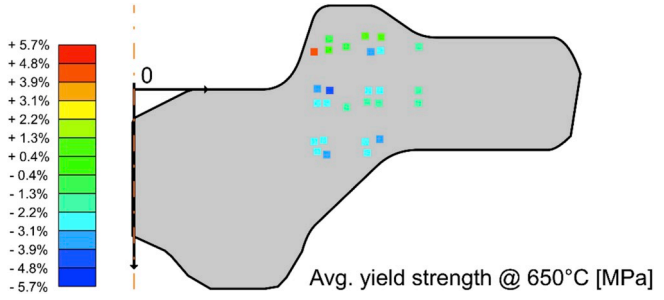

Fig. 2. Selected points of interest of thermo-kinetic modelling of the average standardized yield strength at 650 °C.

Table 1
Chemical composition of Alloy 718 studied in this work.

at.%	Ni	Fe	Cr	Nb	Mo	Ti	Al	C	B
Nominal	53.4	19.2	20.1	3.3	1.8	1.15	1.08	0.01	0.002
High-HV10 (ICP-AES)	53.8	18.1	20.3	3.5	1.9	1.15	1.26	0.09	0
Low-HV0 (ICP-AES)	54.1	17.9	20.2	3.5	1.8	1.15	1.26	0.09	0
High-HV10 (APM)	48.3	17.8	18.3	5.9	3.9	2.3	1.5	2.5	11.5
	±0.8	±0.7	±1.9	±0.9	±1.9	±0.2	±0.2	±0.7 x 10^{-3}	±4.9 x 10^{-3}
Low-HV10 (APM)	49.2	19.6	20.3	4.7	1.7	2.3	1.2	3.0	13.3
	±0.7	±0.3	±0.7	±0.1	±0.2	±0.1	±0.1	±1.4 x 10^{-3}	±6.6 x 10^{-3}

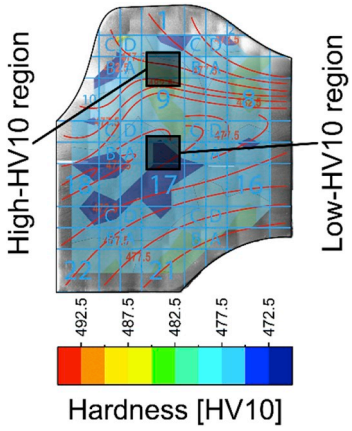

Fig. 3. Stereo-microscope image and overlay hardness map of disk #1. Low-HV10 regions coincide with bent grain flow.

microstructural evolution during thermo-mechanical treatment [10].

2.3. Microstructure characterization

The microstructure of all three plane-parallel cross-sectional turbine disk slices was analyzed using LOM, hardness mapping, SEM and EBSD. The front side was prepared using standard metallographic routines to achieve a scratch-free 3 μm polish. A STRUERS Duramin-300 with ecos 4.30.4.0 software was used for Vickers hardness HV10 testing at ambient temperature. The testing pattern had a 0.5-inch grid distance and five HV10 indents per crossway considering the ASTM standard E92-82. The hardness maps (e.g. Fig. 3) were positioned in the proximity of experimentally obtained local high-temperature yield strength at 650 °C test points. Tensile testing samples were taken in tangential direction in agreement with the ASTM standard E8 from turbine disks ready for delivery and were positioned in the regions of simulated low- and high-yield strength (e.g. Fig. 2). For macro-etching, the front side was polished to 1 μm scratch-free and etched immediately after polishing with water-free Kalling's reagent for ~3 min until the grain flow became visible. The surface was mapped with a M205A stereo-microscope by Leica, and images were stitched together using ImageJ FIJI and the MosaicJ plugin [20,21].

High- and low-HV10 regions were isolated as shown in Fig. 3 via cutting the cross-sectional turbine disks into smaller pieces. Preparation for LOM followed standard metallography routines. Grain boundary etching was achieved with water-free Kalling's reagent for ~1 min. Images were recorded with a Nikon Eclipse ME600 microscope. The grain size was determined with ImageJ FIJI using the linear intercept method according to the ASTM standard E112-12.

Samples were prepared for SEM with final 0.05 μm colloidal OPU polish for ~10 min or electropolishing using a STRUERS Lectropol-5 with STRUERS A2 electrolyte. For SEM images, a ZEISS Auriga cross-beam SEM was used with an accelerating voltage of 20 kV and a 60 μm aperture in high current mode, at a working distance of 7 mm. The backscattered electron (BSE) contrast was used to image the δ-phase and the In-Lens detector was used to resolve γ′- and γ"-precipitates. EBSD grain size measurements used a Hikari Super system attached to a JEOL 7001F SEM with a size '4' aperture (Current: '13') at a working distance of 15 mm. The grain maps were 250 × 250 μm^2 with a step size of 250 nm. The camera binning was 8 × 8 with an exposure of 1.7 ms and gain of 591. Subsequently, a grain dilation clean-up was performed with the EDAX TSL OIM Analysis 8 software. GND density maps were recorded covering an area of 75 × 75 μm^2 with a step size of 75 nm. The camera binning was 4 × 4 with an exposure of 3.4 ms and a gain of 700. Subsequently, a neighbor correlation clean-up was performed with level 3, grain tolerance angle of 5°, and minimum confidence index of 0.1. In a second step, a Kuwahara-filter was applied for every third neighbor in first iteration and a maximum misorientation of 5°. The GND density calculation was based on a software pre-set developed by Field et al. [22].

Disk #1 was then selected for further high-resolution characterization of high-versus low- HV10 regions by TEM and APM. Initially, the bulk chemical composition of both regions was determined by inductively coupled plasma atomic emission spectroscopy (ICP-AES).

TEM foils were ground to 4,000 grid and a thickness of 50 μm after disk punching using standard techniques. The samples were then electropolished using a STRUERS Tenupol-5 with a cooled STRUERS A2 electrolyte at ~11 °C. A JEOL JEM F-200 TEM was used at 200 kV for brightfield and darkfield imaging.

Samples for APM were prepared by cutting and electropolishing using standard techniques [23]. LEAP 3000 and LEAP 4000X Si straight flight path atom probes by CAMECA were used for voltage-mode and laser-assisted data acquisition, respectively. Voltage-mode parameters were 50 K temperature, 20% pulse fraction, and 200 kHz pulse frequency with an evaporation rate of 1.0%. Laser-assisted acquisition parameters were 50 K temperature, 50 pJ laser energy, 200 kHz pulse frequency with an evaporation rate of 1.0% [9,17]. Data analysis was performed using the CAMECA IVAS 3.6.6 software. Data calibration and analysis was carried out using the enhanced iso-surface method and interface methods as introduced elsewhere [17]. For each low- and high-HV10 region, two APM datasets were evaluated in full size and cropped to a cylindrical volume of 25 × 25 × 300 nm^3 for chemical composition and interface method analyses. Two (full size, no cropping) atom probe datasets were evaluated for each high- and low-HV10 region to calculate the γ′- and γ"-precipitate volume fractions, particle radii, and particle number densities.

3. Results

3.1. FEM modelling

Fig. 2 summarizes the modelling results of selected points of interest positioned around typical circumferential low yield-strength regions. The average yield strength shown here is standardized to protect our industrial partner's interests and is significantly reduced by −5.7% in the mid-radius region. The modelled yield strength results were compared to mechanical testing data obtained from various other disks. Modelling results concerning grain boundary strengthening, δ-phase, γ′- and γ"-precipitate volume fractions as well as local temperature and strain are provided in Fig. S1 in the supplementary.

3.2. Hardness maps & macro-etching

Fig. 3 provides a superimposed image of a stereo-microscope image and hardness map (see Supplementary Fig. S2). The hardness mapping grid is added as a blue overlay, and the grain flow is shown in red. While regions denoted as 1, 8, 16 and 21 exhibit a stretched grain flow, regions 9 and 17 in the center show a curved grain flow. Hardness values range from blue to red between 472.5 HV10 and 492.5 HV10. The average hardness of this turbine disk is 478.0 ± 4.5 HV10. The low-HV10 region of 472.5 HV10 in the center is below the standard deviation. The other examined turbine disks show similar low-HV10 regions independently from varying forging geometry, and their properties are summarized in Table 2. Low-HV10 regions coincide with a bent grain flow and are assigned to the low yield strength regions in Fig. 2.

Average hardness and low-HV10 regions may vary between the disks, but all low-HV10 regions fall below the standard deviation and 95% confidence interval as shown in Table 2. However, low-HV10 regions coincide with regions of low yield strength as predicted by modelling, and those coincide with the same areas identified by mechanical testing of other turbine disks.

Table 2
Overview of mechanical properties for all three turbine disk cross-sections.

Disk	#1	#2	#3
Average ± standard deviation [HV10]	478.0 ± 4.5	467.5 ± 5.5	471.5 ± 9.5
95% Confidence interval [HV10]	476.0; 480.0	465.0; 470.0	467.0; 476.0
Low-HV10 region [HV10]	472.5	460.0	462.5

Disk #1 was selected for further, more detailed studies. The bulk chemical composition was determined by ICP-AES analysis. The results provide no significant differences between high- and low-HV10 regions in Table 1.

3.3. Microstructure characterization

3.3.1. Grain size & δ-phase characterization

Fig. 4a) and b) show exemplarily EBSD grain maps after neglecting twin boundaries and the average grain sizes are shown in Table 3. Significantly larger average grain diameters are confirmed in the low-HV10 regions and LOM images are provided in the Supplementary Fig. S3.

Representative SEM micrographs of the δ-phase are provided in Fig. 4c) and d). The δ-phase appears as bright platelets decorating grain and twin boundaries, and occasionally the grain interior. The δ-phase particle sizes and volume fractions are significantly lower in the low-HV10 regions of all three turbine disks and are summarized in Table 3.

3.3.2. Geometrically necessary dislocation density

The GND density was determined using high-resolution EBSD. The inverse pole figure (IPF) maps after clean-up procedures are shown in Supplementary Fig. S4. GND maps are provided in Fig. 5a) and b) and the GND densities for all three turbine disks are summarized in Table 4. The average GND densities for disk #1 are $80 \pm 13 \times 10^{12}$ m^{-2} in the high-HV10 region and $59 \pm 10 \times 10^{12}$ m^{-2} in the low-HV10 region within a 95% confidence interval.

The observed GND densities may represent only a fraction of the absolute dislocation density and allow no quantification. However, qualitative comparison in Table 4 shows lower GND densities in the low-HV10 regions in all three disks.

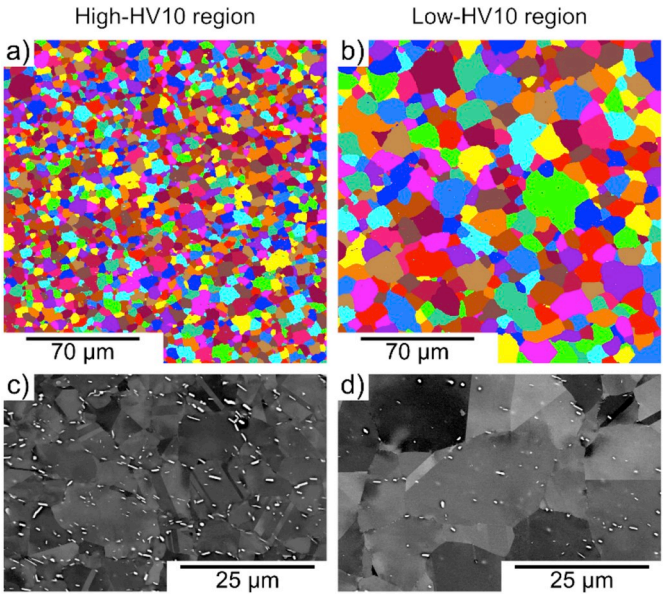

Fig. 4. a) and b) EBSD grain maps disregarding twin boundaries. c) and d) BSE-SEM images show the δ-phase as bright platelets decorating grain and twin boundaries.

Table 3
Grain sizes, δ-phase particle sizes and volume fractions in low- and high-HV10 regions.

Disk	Region	Grain size LOM		Grain size EBSD		δ-phase	
		[µm]	ASTM	[µm]	ASTM	Particle size [µm^2]	Volume fraction [vol. %]
#1	High-HV10	7.3 ± 0.3	11.5	7.0 ± 1.4	11.5	0.19 ± 0.01	2.87 ± 0.07
	Low-HV10	10.9 ± 0.8	9	15.4 ± 3.3	9	0.17 ± 0.01	1.53 ± 0.09
#2	High-HV10	8.3 ± 1.4	11	8.5 ± 3.2	11	0.47 ± 0.02	2.14 ± 0.25
	Low-HV10	12.5 ± 0.8	9.5	15.0 ± 5.8	9	0.48 ± 0.03	1.83 ± 0.39
#3	High-HV10	9.6 ± 0.4	10.5	11.6 ± 4.9	10	0.46 ± 0.02	3.58 ± 0.29
	Low-HV10	12.9 ± 0.9	9.5	18.8 ± 8.5	8.5	0.39 ± 0.02	2.90 ± 0.31

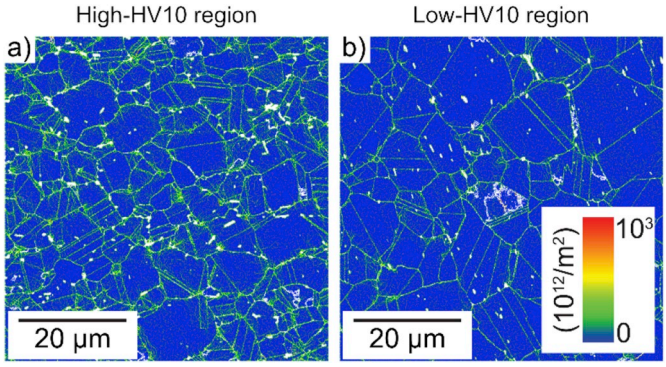

Fig. 5. a) and b) GND density maps of disk #1.

Table 4
GND densities and correlating 95% confidence intervals.

	Region	Disk #1	#2	#3
GND density [10^{12} m^{-2}]	High-HV10	80 ± 67	65 ± 61	79 ± 71
	Low-HV10	59 ± 47	49 ± 47	58 ± 64
95% Confidence interval	High-HV10	67; 93	53; 77	65; 93
	Low-HV10	49; 69	40; 58	45; 71

3.3.3. Precipitate characterization

Electropolished samples were used for high-resolution SEM characterization in Supplementary Fig. S5. Qualitatively, the low-HV10 region exhibits a somewhat higher number of coarsened precipitates. One may note that larger precipitates appear to be aligned on sub-grain boundaries or dislocation cell walls.

Fig. 6a) and b) show the bright-field TEM images of γ′- and γ"-precipitates in {011} orientation. Coprecipitation is obvious, but a distinction between γ′- and γ"-precipitates is not straightforward. The precipitates in Fig. 6a) are densely arranged and small, whereas precipitates in Fig. 6b) are less densely arranged and coarser. Dark-field imaging in Fig. 6c) and d) improves the contrast between γ′- and γ"-precipitates and γ-matrix. In this orientation, the selected area electron diffraction pattern insets show superlattice reflections used to illuminate precipitates only in the two-beam condition. However, overlapping superlattice reflections allow no distinction between γ′- and γ"-precipitates.

APM allows quantitative differentiation of γ′- and γ"-precipitates with quasi-atomic resolution [17,23]. Fig. 7a) and b) provide two representative reconstructions from the high- and low-HV10 regions in disk #1. Based on enrichments in Al and Ti, or Nb, γ′- and γ"-precipitates

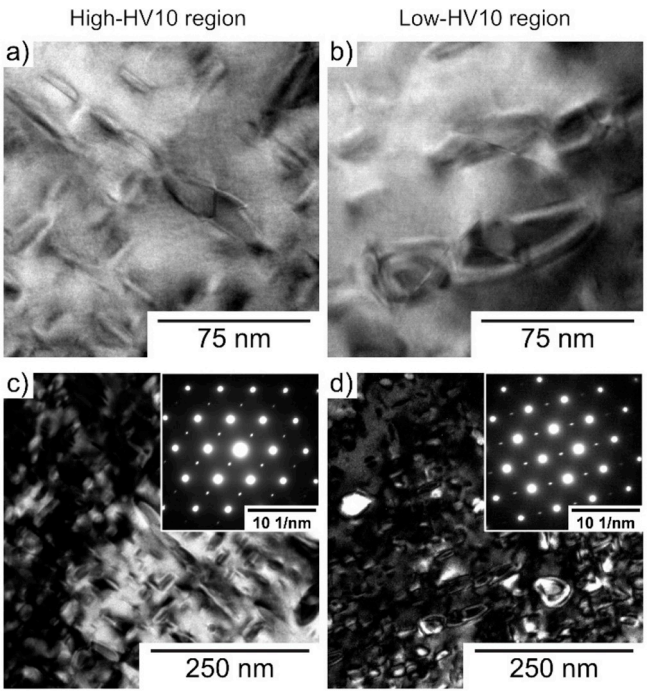

Fig. 6. a) and b) bright-field TEM images. c) and d) dark-field TEM images and corresponding diffraction patterns as insets.

are represented by turquoise or brown iso-surfaces, respectively. Previously determined, suitable iso-surface threshold values were 10.5 at.% Al + Ti and 13.0 at.% for γ′- and γ"-precipitates, respectively [9,17]. The average bulk chemical composition of the γ-matrix, and γ′- and γ"-precipitates in Table 1 is based on ranged ions only, and shows enrichments in Nb, and Mo, and depletions of Fe and Cr in the high-HV10 region.

APM data of the high-HV10 region in Fig. 7a) and Supplementary Video 1 show a comparably large γ"-precipitate, smaller γ′-γ" duplet and triplet coprecipitates and monolithic γ′- and γ"-precipitates. Fig. 7b) and Supplementary Video 2 show less densely arranged γ′- and γ"-precipitates with larger particle radii in the low-HV10 region. Note that all atoms are blanked out and only iso-surfaces are represented here. This precipitate morphology is similar to the TEM images in Fig. 6a) and b). The detailed volume fraction, particle radius and particle density are provided in Table 5. In the low-HV10 region, γ′-precipitate volume fraction and average γ′- and γ"-precipitate particle radii are increased, while the γ′- and γ"-precipitate particle density is lower. The graphical comparison of these precipitate properties is shown in Fig. 8.

Supplementary videos related to this article can be found at https://doi.org/10.1016/j.msea.2020.138967.

The precipitate morphologies are classified into γ′- and γ"-precipitate monoliths, duplets, γ"-γ′-γ" or γ′-γ"-γ′ triplets, and quadruplets, based on the interface method introduced in earlier work [17]. The precipitate morphology fractions are provided in Table 6 and a graphic representation is provided in Fig. 9.

The fraction of each precipitate morphology class in relation to the absolute number of precipitates per dataset is determined as follows: The fraction of γ′-precipitate monoliths in the low-HV10 region is significantly reduced to 14.9 ± 4.4% in comparison to 26.2 ± 2.5% in the high-HV10 region. Instead, the fraction of γ′-γ"-γ′ triplets in the low-HV10 region is increased to 18.3 ± 5.1%, in comparison to 8.7 ± 2.2% in the high-HV10 region. This indicates the predominance of simple monolith and duplet morphologies in the high-HV10 region, and more complex (triplet, quadruplet) morphologies in the low-HV10 region.

Comparing high- and low-HV10 regions in Fig. 8, the γ′-precipitate volume fraction is increased from 12.2 to 14.5 vol.% while the γ"-precipitate volume fraction remains constant (Fig. 8a)). The average particle radius in the low-HV10 region in Fig. 8b) is increased for γ′- and γ"-precipitates by approximately 10%. In contrast, Fig. 8c) shows that the particle density in the low-HV10 regions is reduced for γ′- and γ"-precipitates by 30%. A correlation plot of the chemical composition in Supplementary Fig. S6 shows a graphical representation of the increased concentration of Mo and Nb in the high-HV10 region by 2.2 at.%, 1.2 at.%, respectively.

Comparing the precipitate morphology classes between high- and low-HV10 regions in Fig. 9, the most significant differences can be noted for the γ′-precipitate monoliths, duplets, and γ′-γ"-γ′ triplets.

4. Discussion

4.1. Modelling

The modelling results presented in Fig. 2 and Supplementary Fig. S1 are comparable to the experimental results in Tables 2, 3 and 5. Locally reduced grain boundary strengthening correlates well with coarse grains in the low-HV10 region. The δ-phase fraction is reduced in the same

Table 5
Overview of γ′- and γ"-precipitate volume fraction, particle radius and particle density.

Precipitate properties	Volume fraction [vol. %]		Particle radius [nm]		Particle density [10^{23} m^{-3}]	
	γ′	γ"	γ′	γ"	γ′	γ"
High-HV10	12.2 ± 0.4	23.8 ± 0.5	5.8 ± 0.3	7.1 ± 0.9	3.02 ± 0.51	2.79 ± 0.74
Low-HV10	14.5 ± 0.1	23.3 ± 0.1	6.5 ± 0.2	7.6 ± 0.4	2.02 ± 0.83	2.06 ± 0.65

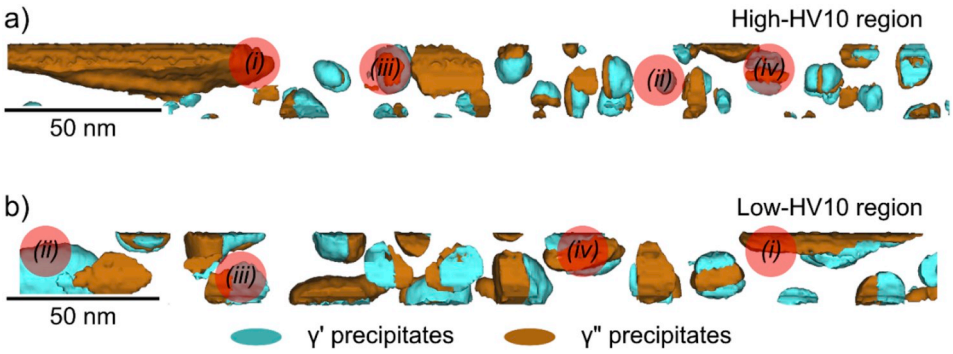

Fig. 7. Cropped APM reconstruction for two exemplary datasets from disk #1 of a) high-HV10 region and b) low-HV10 region with coarsened γ" precipitates (i), smaller γ′- and γ"-precipitate monoliths (ii), duplets (iii) and triplets (iv). Atoms are blanked out, and only iso-surfaces for γ′- and γ"-precipitates are shown to improve visualization.

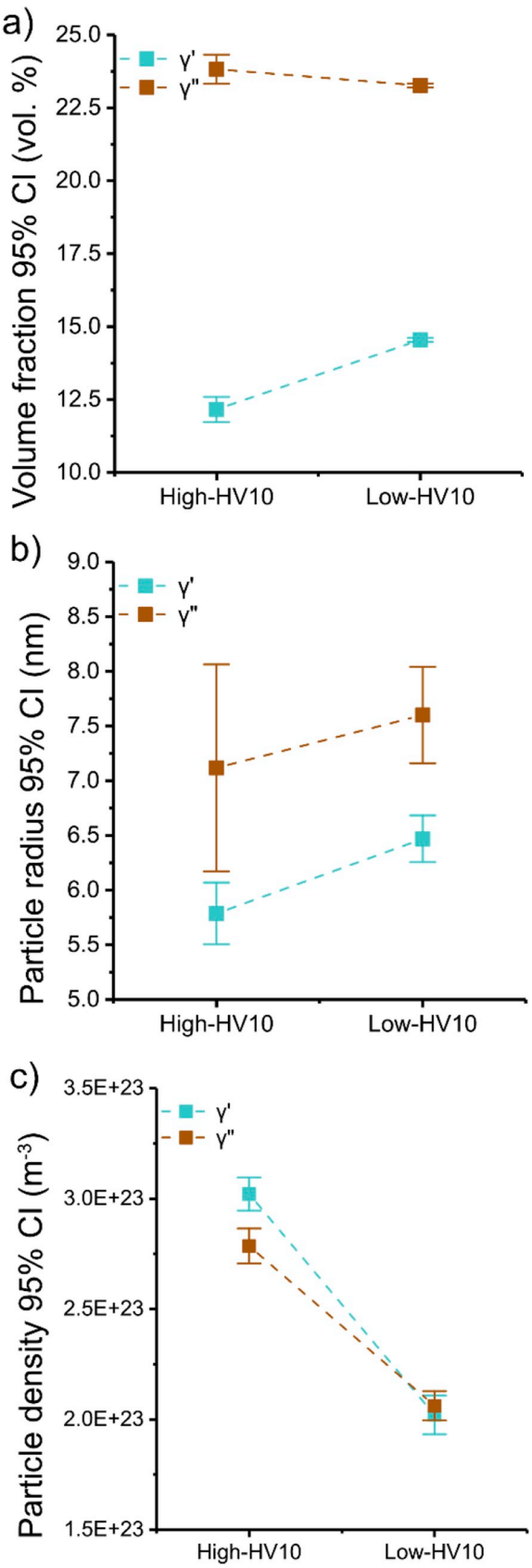

Fig. 8. APM γ′- and γ"-precipitate statistics a) volume fraction, b) particle radii, c) particle density.

Table 6
Fraction of monoliths, duplets, triplets and quadruplets in high- and low-HV10 regions.

Precipitate morphology	Monoliths [%]		Duplets [%]	Triplets [%]		Quadruplets [%]
	γ′	γ"		γ"-γ′-γ"	γ′-γ"-γ′	
High-HV10	26.2 ± 2.5	20.0 ± 2.9	40.5 ± 4.9	2.6 ± 0.9	8.7 ± 2.2	2.1 ± 0.9
Low-HV10	14.9 ± 4.4	27.0 ± 11.5	32.4 ± 7.1	4.8 ± 2.6	18.3 ± 5.1	2.7 ± 1.4

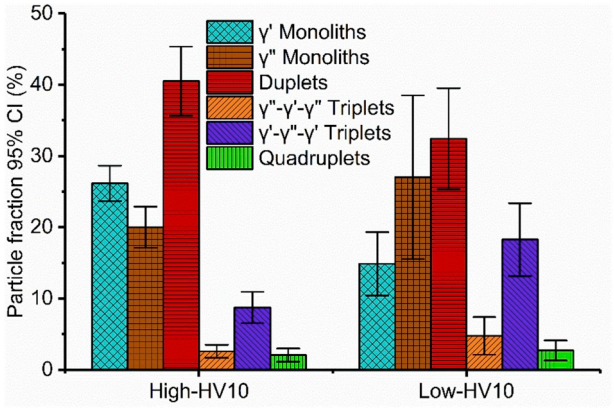

Fig. 9. Fractions of monoliths, duplets, triplets, and quadruplets in the high- and low-HV10 regions of disk #1.

region for both modelled and experimental data. Supplementary Fig. S1 suggests a decrease in the γ′-precipitate volume fraction and an increase in the γ"-precipitate volume fraction, the opposite trend was found via APM. However, the γ"-precipitate volume fraction is significantly larger than the γ′-precipitate volume fraction in both experimental and modelled data. The local temperature and strain provide high values correlating with the experimental low-HV10 region. The locally reduced yield strength in Fig. 2 correlates well with experimental values and hardness mapping in Fig. 3.

4.2. Microstructure and properties

The macroscopic grain flow in Fig. 3 commonly follows the component contour in forged superalloy turbine disks [6,7]. Low-HV10 regions were successfully identified in all three disks, although HV10 is only a qualitative yield strength indicator. However, HV10 mapping at ambient temperature and yield strength obtained by tensile testing at 650 °C correlate well as in Sections 3.1. and 3.2.

Fig. 4 correlates local larger grain size and lower δ-phase volume fraction in low-HV10 regions. Considering Supplementary Fig. S1, the local microstructural evolution is linked to local temperature and strain variations. Coarse grains as found in Fig. 4b) can reduce the hardness according to the Hall-Petch relationship [24,25]. However, differences of less than 3 ASTM grain size classes between high- and low-HV10 regions are insufficient to cause the yield strength and hardness variations in Figs. 2 and 3. Grain refinement in Alloy 718 is facilitated by the δ-phase via Zener pinning [11]. It has also been shown that volume fraction and dispersion are critical for the local grain size [26]. Consequently, changes in the δ-phase volume fraction must precede ageing. Here, three phenomena may require consideration: Firstly, deformation-induced, adiabatic overheating above the δ-solvus temperature. This would exceed geometric restrictions of low-HV10 regions in Fig. 3 and is unlikely. Secondly, inhomogeneities in the pre-material can be caused due to insufficient homogenization. This is plausible but no segregations were found on a macroscopic scale by ICP-AES analysis

in Table 1. Finally, deformation-induced δ-phase dissolution has been observed in Alloy 718 and derivatives before [27,28]. According to He et al. [27], this effect is facilitated by high temperature, high strain and low strain-rate, although the δ-solvus temperature must not necessarily be exceeded. As shown in Fig. 1, disk forging in the present study was carried out well below 1,100 °C and local strain and temperature reached highest values in the low-HV10 region in Supplementary Fig. S1. Local variations in the strain rate may be introduced by the present disk geometry.

4.3. Nanostructure

The nanostructure of dislocations and γ′- and γ"-precipitates determines most of the outstanding strength properties of Alloy 718 [10].

Locally reduced work hardening is demonstrated by the lower GND density in the low-HV10 region in Fig. 5b). Highest strain and temperature were present during forging in this region; thus, this finding may initially appear counterintuitive. However, localized reduction of δ-phase volume fraction (see Table 3) requires consideration the following: Firstly, δ-phase particles in Alloy 718 stabilize smaller grains via grain boundary pinning [11] and are preferred nucleation sites for dynamic recrystallisation (DRX) [29]. Marty et al. proposed a DRX model so that locally reduced δ-phase fraction may result in fewer and larger grains under the consumption of dislocations [29]. As quenching within the disk can be delayed by several seconds, meta-dynamic recrystallisation (MRX) must be considered [30]. Secondly, work hardening is less efficient. The critical role of the δ-phase for dislocation multiplication in Alloy 718 derivatives was demonstrated by Wen et al. [31] using iso-thermal compressive testing. Static recrystallisation is not considered, due to insufficient exposure time and the forging temperatures used in this study.

Figs. 8 and 9 show for the low-HV10 region fewer monolithic γ′-precipitates with increased volume fraction. Both, γ′- and γ"-precipitate show increased particle radii and a lower particle density in the low-HV10 region in Fig. 8. Finally, the chemical composition as per APM shows local depletion of Nb, and Mo, and enrichment in Fe and Cr in the low-HV10 region, contradicting initial findings via ICP-AES in Table 1. These local variations in Nb may originate from coarsened γ"-precipitates not being captured in the APM datasets in Fig. 7. While local fluctuations in the Nb concentration are obvious due to the γ"-precipitate stoichiometry $Ni_3(Nb)$, partial solubility of Al in γ"-precipitates as found by Miller et al. [32] may has the same effect. The increase in Mo is an APM artefact due to the proximity of low-intensity Mo^{3+} peaks to stronger Ni^{2+} and Nb^{3+} peaks [33,34]. Small changes in Fe and Cr are assumed to have no significant influence on γ′- and γ"-precipitates.

Alloy 718 is primarily strengthened by γ"-precipitates, thus, the increased volume fraction of γ′-precipitates in the low-HV10 region may only have a minor impact on the properties [13]. Considering the morphology classes presented in Fig. 9, γ′-precipitates are predominantly found as γ′-γ"-γ′ triplets, and this will influence their strain fields. Based on phase field modelling and FEM modelling, γ"-precipitates have been found to induce tensile strains and γ′-precipitates compressive strains into the surrounding γ-matrix of Alloy 718 and Alloy 706 [35,36]. Depending on the detailed coprecipitate configuration, interaction with passing dislocations is altered [36].

Further, γ′- and γ"-precipitate dispersion and particle sizes influence the high-temperature yield strength [37]. As shown in Table 5 and Fig. 8, γ"-precipitates exhibit a larger particle radius in the low-HV10 region. Precipitates with radii >25 nm lose coherency and their strengthening effect [38]. Supplementary Fig. S7 shows larger radii for γ′- and γ"-precipitates in the low-HV10 region. Due to the lower GND density, fewer nucleation sites are available and γ"-precipitate coarsening is accelerated. The sensitivity of γ"-precipitates to dislocations has been shown in previous studies [38–40]. Coarsening of γ′- and γ"-precipitates follows the Lifshitz-Slyozof-Wagner (LSW) theory, whereas only γ"-precipitates depend on the Nb diffusivity [38,41,42].

Further insight into the precipitation mechanism is derived from the particle morphologies in low- and high-HV10 regions in Fig. 8. The dominance of γ′-γ"-γ′ over γ"-γ′-γ" is an indicator for the DA effect [9,17]. However, the low-HV10 region exhibits a significantly higher fraction of triplets with fewer monolithic γ′- and γ"-precipitates. While GND density and Nb in solid solution have been identified as critical [9], the present study provides evidence for further sensitivity of γ′- and γ"-precipitates to local processing parameters during DA of Alloy 718.

4.4. Process-microstructure relationship

Based on the microstructural differences between high- and low-HV10 regions in radial positions, a qualitative model is derived in Fig. 10, providing insight into the origins of yield strength variations in forged turbine disks. The occurrence of high- and low-HV10 regions in all three disks indicates that they are independent of the forging geometry. The upper and lower branches of Fig. 10 represent low- and high-HV10 regions, respectively.

In the lower branch, moderate temperature and strain have a minor effect on the δ-phase volume fraction. A high dislocation density is retained from forging via grain boundary pinning. Assuming primary γ"-nucleation, the high dislocation density provides abundant heterogeneous nucleation sites for γ"-precipitates during DA and particle growth is controlled by Nb diffusion. This results in small precipitate radii, high particle density and higher number of monolithic precipitates.

The upper branch represents local high temperatures and strain, below the δ-solvus temperature. Strain-induced δ-phase dissolution reduces the δ-phase volume fraction and increases Nb in solid solution in the proximity of δ-phase particles during forging. Immediate DRX followed by MRX consumes dislocations during grain coarsening due to insufficient grain boundary pinning. Consequently, these areas exhibit coarser grains and lower dislocation densities. Fewer nucleation sites and higher Nb concentration in solid solution accelerate γ"-precipitate coarsening during DA. This results in large particle radii, lower particle density and more complex particle morphologies such as triplets.

However, although not overserved by ICP-AES in this study, Nb segregation in the pre-material must be considered as potential origin for yield strength variations. Typical forging heats may result in rotational symmetric strain-induced δ-phase dissolution, but circumferential yield strength variations do not necessary follow rotational symmetry. Homogenization treatment, or billet conversion parameters may be considered as potential causes in the pre-material processing. However, this is beyond the scope of the present study.

5. Conclusions

This study connects macroscopically occurring yield strength variations in directly aged turbine disks with changes in the micro- and nanostructure of Alloy 718 in a qualitative microstructural model. We provide the following conclusions:

- Localized strain-induced δ-phase dissolution and inhomogeneities in the pre-material must be considered during direct ageing of Alloy 718 turbine disks in order to avoid local high temperature yield strength variations. These variations are successfully correlated to hardness mappings via a comprehensive modelling and experimental approach.
- Direct ageing introduces new, complex processing-microstructure-properties relationships influencing grain size, δ-phase, GND density, and γ′- and γ"-precipitate morphologies. Low-HV10 regions exhibit larger grain sizes, lower δ-phase fractions, and lower GND densities. At the nanoscale, these regions exhibit higher volume fractions of γ′-precipitates, larger γ′- and γ"-precipitate radii, lower γ′- and γ"-precipitate particle densities and predominant γ′-γ"-γ′ triplet morphologies.

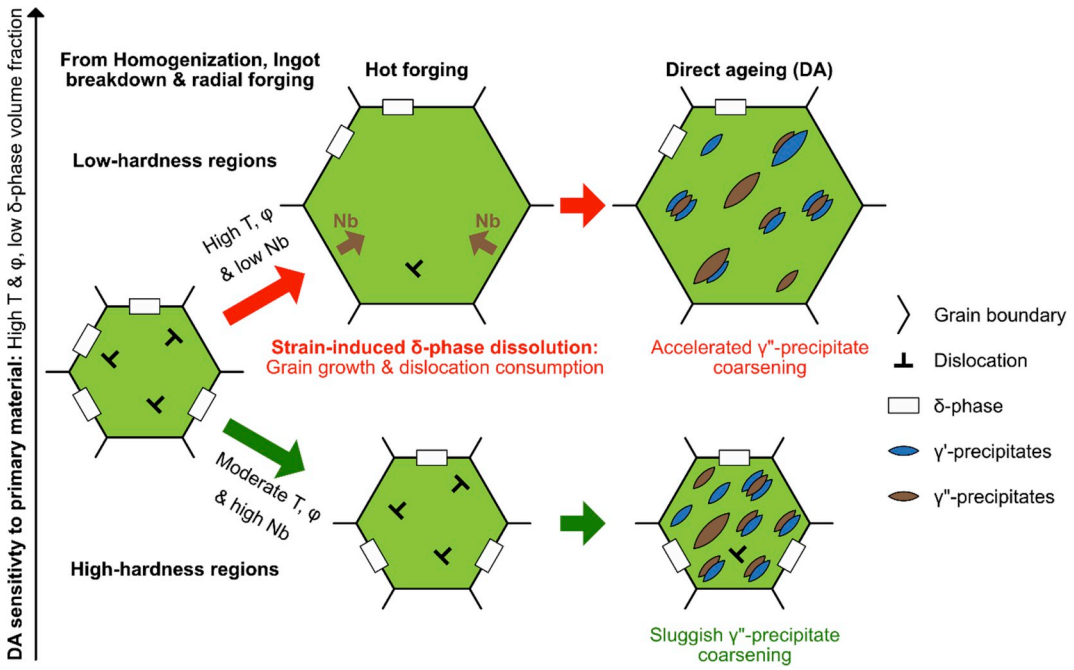

Fig. 10. Qualitative microstructural model for high- and low-HV10 regions. Low-HV10: Areas with locally reduced Nb concentration are more sensitive to strain-induced δ-phase dissolution due to high temperature T and strain ϕ. That grain growth via DRX and MRX consumes dislocations in the γ-matrix. The reduced dislocation density provides fewer nucleation sites and accelerates γ"-precipitate coarsening. High-HV10: Moderate temperature T and strain ϕ with high Nb concentration retain the δ-phase and a high dislocation density from forging, providing more sluggish γ"-precipitate coarsening.

- Forging parameters (temperature and strain) require careful re-evaluation throughout the entire turbine disk manufacturing process to prevent the local deterioration of the direct ageing effect due to accelerated γ"-precipitate coarsening.

However, the following limitations of this study provide the basis for our future work:

- Characterization of forged and aged turbine disks impede the characterization of pre-material inhomogeneities. Thus, further analyses of inhomogeneities during the pre-material manufacturing processes are required. Future work aims to reveal the direct ageing effect as a function of δ-phase fraction in billets.
- A quantitative relationship between processing parameters (temperature, strain), properties (yield strength) and microstructures (grain size, δ-phase, GND density, γ′- and γ"-precipitates) will require systematic through-process studies of directly aged Alloy 718 turbine disk manufacturing, for example in a Gleeble thermo-mechanical simulator.

Data statement

Data will be made available upon reasonable request to the corresponding author.

Declaration of competing interest

The authors declare no conflict of interest.

CRediT authorship contribution statement

F. Theska: Project administration, Writing - original draft, Writing - review & editing, Formal analysis. **A. Stanojevic:** Resources, Software, Writing - review & editing. **B. Oberwinkler:** Resources, Funding acquisition, Writing - review & editing. **S. Primig:** Supervision, Funding acquisition, Writing - review & editing.

Acknowledgements

The authors acknowledge the facilities and the scientific and technical assistance of the Microscopy Australia team at the Electron Microscope Unit (EMU), UNSW Sydney, and at Sydney Microscopy & Microanalysis at The University of Sydney. The authors are grateful for the technical assistance of Drs Richard Webster (TEM, UNSW) and Takanori Sato (APM, Sydney) and scientific discussions with Prof Simon P. Ringer (Sydney) and Dr Flora Godor (voestalpine BÖHLER Aerospace). Contributions by Mr Ethan D. Hill (North Carolina State University) were supported through the U.S. National Science Foundation under the award number OISE-1357113. Dr Sophie Primig acknowledges gratefully research funding from the Australian Research Council (ARC) via her DECRA Fellowship (DE180100440) and the UNSW Scientia Fellowship Schemes.

Appendix A. Supplementary data

Supplementary data to this article can be found online at https://doi.org/10.1016/j.msea.2020.138967.

References

[1] R. Parker, G. Fedder, Aircraft engines: a proud heritage and an exciting future, Aeronaut. J. 120 (2016) 131–169, https://doi.org/10.1017/aer.2015.6.
[2] G. Baxter, P. Srisaeng, G. Wild, A cross sectional study of the ten longest ultra-long-range air routes, Transp. Telecommun. J. 20 (2019) 162–174, https://doi.org/10.2478/ttj-2019-0015.
[3] A. Dik, N. Bitén, V. Zaccaria, I. Aslanidou, K.G. Kyprianidis, Conceptual design of a 3-shaft turbofan engine with reduced fuel consumption for 2025, Energy Procedia 142 (2017) 1728–1735, https://doi.org/10.1016/j.egypro.2017.12.556.
[4] V.F. da Fonseca Filho, R.F. Gama Ribeiro, P.T. Lacava, Turbofan engine performance optimization based on aircraft cruise thrust level, J. Braz. Soc. Mech. Sci. Eng. 41 (2019) 64, https://doi.org/10.1007/s40430-018-1562-1.
[5] Airbus Group Se, Global Market Forecast - Global Networks, Global Citizens 2018-2037, 2018.
[6] M.J. Donachie, Superalloys: A Technical Guide, second ed., ASM International, Ohio, 2002 doi:10.1361.
[7] R.C. Reed, The Superalloys Fundamentals and Applications, Cambridge, Cambridge University Press, Cambridge, 2006.

[8] D.F. Paulonis, J.J. Schirra, Alloy 718 at Pratt & Whitney: historical perspective and future challenges, in: Superalloys 718, 625, 706 Var. Deriv, 2001, https://doi.org/10.7449/2001/Superalloys_2001_13_23.
[9] F. Theska, A. Stanojevic, B. Oberwinkler, S.P. Ringer, S. Primig, On conventional versus direct ageing of Alloy 718, Acta Mater. 156 (2018) 116–124, https://doi.org/10.1016/j.actamat.2018.06.034.
[10] B. Oberwinkler, A. Fischersworring-Bunk, M. Hüller, M. Stockinger, Integrated process modeling for the mechanical properties optimization of direct aged alloy 718 engine disks, in: Superalloys 2016, John Wiley & Sons, Inc., Hoboken, NJ, USA, 2016, pp. 513–521, https://doi.org/10.1002/9781119075646.ch55.
[11] M. Anderson, A.L. Thielin, F. Bridier, P. Bocher, J. Savoie, δ Phase precipitation in Inconel 718 and associated mechanical properties, Mater. Sci. Eng. A 679 (2017) 48–55, https://doi.org/10.1016/j.msea.2016.09.114.
[12] A. Drexler, B. Oberwinkler, S. Primig, C. Turk, E. Povoden-Karadeniz, A. Heinemann, W. Ecker, M. Stockinger, Experimental and numerical investigations of the γ'' and γ' precipitation kinetics in Alloy 718, Mater. Sci. Eng. A 723 (2018) 314–323, https://doi.org/10.1016/j.msea.2018.03.013.
[13] J.M. Oblak, D.F. Paulonis, D.S. Duvall, Coherency strengthening in Ni base alloys hardened by DO22 Gamma Double Prime precipitates, Metall. Trans. 5 (1974) 143–153.
[14] R. Cozar, A. Pineau, Morphology of γ' and γ'' precipitates and thermal stability of Inconel 718 type alloys, Metall. Trans. 4 (1973) 47–59, https://doi.org/10.1007/BF02649604.
[15] M. Sundararaman, P. Mukhopadhyay, S. Banerjee, Precipitation of the δ-Ni3Nb phase in two nickel base superalloys, Metall. Trans. A 19 (1988) 453–465, https://doi.org/10.1007/BF02649259.
[16] D.D. Krueger, The development of direct age 718 for gas turbine engine disk applications, in: Superalloys 718 Metall. Appl, TMS, 1989, pp. 279–296, https://doi.org/10.7449/1989/Superalloys_1989_279_296.
[17] F. Theska, S.P. Ringer, S. Primig, Atom probe microscopy of strengthening effects in alloy 718, Microsc. Microanal. (2019) 1–11, https://doi.org/10.1017/S1431927618015611.
[18] E. Kozeschnik, Modeling Solid-State Precipitation, 2013, https://doi.org/10.5643/9781606500644.
[19] U. Ayachit, The ParaView Guide: A Parallel Visualization Application, 2015 doi:citeulike-article-id:4375994.
[20] J. Schindelin, I. Arganda-Carreras, E. Frise, V. Kaynig, M. Longair, T. Pietzsch, S. Preibisch, C. Rueden, S. Saalfeld, B. Schmid, J.-Y. Tinevez, D.J. White, V. Hartenstein, K. Eliceiri, P. Tomancak, A. Cardona, Fiji: an open-source platform for biological-image analysis, Nat. Methods 9 (2012) 676–682, https://doi.org/10.1038/nmeth.2019.
[21] P. Thévenaz, M. Unser, User-friendly semiautomated assembly of accurate image mosaics in microscopy, Microsc. Res. Tech. (2007), https://doi.org/10.1002/jemt.20393.
[22] D.P. Field, P.B. Trivedi, S.I. Wright, M. Kumar, Analysis of local orientation gradients in deformed single crystals, Ultramicroscopy 103 (2005) 33–39, https://doi.org/10.1016/j.ultramic.2004.11.016.
[23] B. Gault, M.P. Moody, J.M. Cairney, S.P. Ringer, Atom Probe Microscopy, Springer, New York, New York, NY, 2012, https://doi.org/10.1007/978-1-4614-3436-8.
[24] E.O. Hall, The deformation and ageing of mild steel III Discussion of results, Proc. Phys. Soc. B (1951), https://doi.org/10.1088/0370-1301/64/9/303.
[25] N.J. Petch, The cleavage strength of polycrystals, J. Iron Steel Inst. 173 (5) (1953) 25–28.
[26] A. Agnoli, M. Bernacki, R. Logé, J.-M. Franchet, J. Laigo, N. Bozzolo, Understanding and modeling of grain boundary pinning in Inconel 718, in: Superalloys 2012, John Wiley & Sons, Inc., Hoboken, NJ, USA, 2012, pp. 73–82, https://doi.org/10.1002/9781118516430.ch8.
[27] D.G. He, Y.C. Lin, X.Y. Jiang, L.X. Yin, L.H. Wang, Q. Wu, Dissolution mechanisms and kinetics of δ phase in an aged Ni-based superalloy in hot deformation process, Mater. Des. 156 (2018) 262–271, https://doi.org/10.1016/j.matdes.2018.06.058.
[28] B. Hassan, J. Corney, Grain boundary precipitation in Inconel 718 and ATI 718Plus, Mater. Sci. Technol. 33 (2017) 1879–1889, https://doi.org/10.1080/02670836.2017.1333222.
[29] B. Marty, J.Y. Guedou, P. Gergaud, J.L. Lebrun, Recrystallization and work-hardening prediction during forging process of Inconel 718, in: Superalloys 718, 625, 706 Var. Deriv, TMS, 1997, pp. 331–342, https://doi.org/10.7449/1997/Superalloys_1997_331_342.
[30] A. Stanojevic, C. Bucher, M. Gruber, B. Oberwinkler, M. Stockinger, Optimization of the Forging Process Window in Respect of AGG, IGG and Direct Age Effect in Alloy 718 Engine Disks, 2018, pp. 691–709, https://doi.org/10.1007/978-3-319-89480-5_46.
[31] D.X. Wen, Y.C. Lin, Y. Zhou, A new dynamic recrystallization kinetics model for a Nb containing Ni-Fe-Cr-base superalloy considering influences of initial δ phase, Vacuum 141 (2017) 316–327, https://doi.org/10.1016/j.vacuum.2017.04.030.
[32] M.K. Miller, S.S. Babu, M.G. Burke, Comparison of the phase compositions in Alloy 718 measured by atom probe tomography and predicted by thermodynamic calculations, Mater. Sci. Eng. A 327 (2002) 84–88, https://doi.org/10.1016/S0921-5093(01)01881-0.
[33] G. Sha, S.P. Ringer, Effect of laser pulsing on the composition measurement of an Al-Mg-Si-Cu alloy using three-dimensional atom probe, Ultramicroscopy (2009), https://doi.org/10.1016/j.ultramic.2008.10.012.
[34] F. Liu, H.-O. Andrén, Effects of laser pulsing on analysis of steels by atom probe tomography, Ultramicroscopy 111 (2011) 633–641, https://doi.org/10.1016/j.ultramic.2010.12.012.
[35] V. Kindrachuk, N. Wanderka, J. Banhart, γ′/γ″ Co-precipitation in Inconel 706 alloy: a 3D finite element study, Mater. Sci. Eng. A 417 (2006) 82–89, https://doi.org/10.1016/j.msea.2005.10.062.
[36] D. McAllister, D. Lv, H. Deutchman, B. Peterson, Y. Wang, M.J. Mills, Characterization and modeling of deformation mechanisms in Ni-base superalloy 718, in: Superalloys 2016, 2016, https://doi.org/10.1002/9781119075646.ch88.
[37] M.R. Ahmadi, E. Povoden-Karadeniz, K.I. Öksüz, A. Falahati, E. Kozeschnik, A model for precipitation strengthening in multi-particle systems, Comput. Mater. Sci. 91 (2014) 173–186, https://doi.org/10.1016/j.commatsci.2014.04.025.
[38] A. Devaux, L. Nazé, R. Molins, A. Pineau, A. Organista, J.Y. Guédou, J.F. Uginet, P. Héritier, Gamma double prime precipitation kinetic in Alloy 718, Mater. Sci. Eng. A 486 (2008) 117–122, https://doi.org/10.1016/j.msea.2007.08.046.
[39] H. Zhang, C. Li, Q. Guo, Z. Ma, H. Li, Y. Liu, Improving creep resistance of nickel-based superalloy Inconel 718 by tailoring gamma double prime variants, Scripta Mater. 164 (2019) 66–70, https://doi.org/10.1016/j.scriptamat.2019.01.041.
[40] M. Sundararaman, P. Mukhopadhyay, S. Banerjee, Some aspects of the precipitation of metastable intermetallic phases in INCONEL 718, Metall. Trans. A 23 (1992) 2015–2028, https://doi.org/10.1007/BF02647549.
[41] I.M. Lifshitz, V.V. Slyozov, The kinetics of precipitation from supersaturated solid solutions, J. Phys. Chem. Solid. (1961), https://doi.org/10.1016/0022-3697(61)90054-3.
[42] M. Kahlweit, Ostwald ripening of precipitates, Adv. Colloid Interface Sci. (1975), https://doi.org/10.1016/0001-8686(75)85001-9.